The Meteoritical Society

Meteoritics & Planetary Science 43, Nr 1/2, 143–160 (2008)
Abstract available online at http://meteoritics.org

Transmission electron microscopy of cometary residues from micron-sized craters in the Stardust Al foils

Hugues LEROUX[1*], Rhonda M. STROUD[2], Zu Rong DAI[3], Giles A. GRAHAM[3], David TROADEC[4], John P. BRADLEY[3], Nick TESLICH[3], Janet BORG[5], Anton T. KEARSLEY[6], and Friedrich HÖRZ[7]

[1]Laboratoire de Structure et Propriétés de l'Etat Solide, UMR CNRS 8008, Université des Sciences et Technologies de Lille, F-59655 Villeneuve d'Ascq, France
[2]Materials Science and Technology Division, Code 6360, Naval Research Laboratory, 4555 Overlook Avenue SW, Washington, D.C. 20375, USA
[3]Institute for Geophysics and Planetary Physics, Lawrence Livermore National Laboratory, 7000 East Avenue, L-413, Livermore, California 94550, USA
[4]Institut d'Electronique de Microélectronique et de Nanotechnologie, UMR CNRS 8520, Université des Sciences et Technologies de Lille, F-59655 Villeneuve d'Ascq-Cedex, France
[5]Institut d'Astrophysique Spatiale (IAS), Batiment 121, Université Paris-Sud 11 and CNRS (UMR 8617), F-91405 Orsay, France
[6]Impacts and Astromaterials Research Centre, Department of Mineralogy, Natural History Museum, London SW7 5BD, UK
[7]NASA Johnson Space Center, ARES, KR Houston, Texas 77058, USA
*Corresponding author. E-mail: Hugues.Leroux@univ-lille1.fr

(Submitted 03 April 2007; revision accepted 27 July 2007)

Abstract–We report transmission electron microscopy (TEM) investigations of micro-craters that originated from hypervelocity impacts of comet 81P/Wild 2 dust particles on the aluminium foil of the Stardust collector. The craters were selected by scanning electron microscopy (SEM) and then prepared by focused ion beam (FIB) milling techniques in order to provide electron transparent cross-sections for TEM studies. The crater residues contain both amorphous and crystalline materials in varying proportions and compositions. The amorphous component is interpreted as resulting from shock melting during the impact and the crystalline phases as relict minerals. The latter show evidence for shock metamorphism. Based on the residue morphology and the compositional variation, the impacting particles are inferred to have been dominated by mixtures of submicron olivine, pyroxene and Fe sulfide grains, in agreement with prior results of relatively coarse-grained mineral assemblages in the aerogel collector.

INTRODUCTION

The Stardust mission successfully returned dust grains from comet 81P/Wild 2 to Earth for detailed analysis of their mineralogic and compositional characteristics, including isotope systematics and organic compound identification. Although captured by Jupiter into its present orbit only 30 years ago (Sekanina and Yeomans 1985), 81P/Wild 2 is nevertheless an ancient object believed to have formed at the outer edge of the solar nebula, residing for most of geologic history in cold storage beyond Neptune (Brownlee et al. 2006). The particles collected by Stardust should thus represent samples of the least altered solar system materials that preserve and reflect the processes that operated at the outer edges of the solar nebula. The detailed laboratory analysis of these solids should shed light on these processes and, combined with astrophysical models, lead to an improved understanding of the early solar system.

The dust grains emanating from Wild 2 encountered the Stardust spacecraft at 6.1 km/s. The primary dust collecting device consisted of low density, highly porous, SiO_2-based aerogel, which was shown in impact experiments (e.g., Barrett et al. 1992; Burchell et al. 2001, 2006) and in low Earth orbit collections (e.g., Hörz et al. 2000) to trap unmelted residues of silicate projectiles at velocities as high as 7 km/s. Individual tiles of aerogel on Stardust, 20 × 40 mm large and 30 mm deep, resided in a modular grid-like collector tray. Each rib of this modular collector grid was wrapped with a metallic foil, made from soft Al 1100 series alloy (Al 1145), nominally of 104 μm (0.004″) thickness. While the primary purpose of these foils was to aid in the eventual extraction, after return to Earth, of each of the 132 individual aerogel tiles

(Tsou et al. 2004), portions of each foil were exposed during the cometary flyby. The total surface area exposed was 1039 cm^2 of aerogel and 152 cm^2 of Al foil.

Commensurate with the densities of the collector materials, 0.005–0.05 g/cm^3 for the density graded aerogel and 2.7 g/cm^3 for the aluminium, the cometary dust collisions resulted in deep penetration tracks and impact craters, respectively. Both features were expected to yield analyzable projectile materials, albeit in dramatically different forms, consistent with the shock and thermal environment experienced during their capture. The tracks were expected to yield largely unmelted residues, whereas the craters would be lined with projectile melts. While these expectations were substantially correct, it turns out that melting was more severe than expected in the aerogel tracks and conversely, a significant portion of craters in Al foils still contain crystalline materials. The two collector media employed on Stardust are thus highly complementary (e.g., Zolensky et al. 2006; Flynn et al. 2006; Hörz et al. 2006). Indeed, the highly localized lumps of pure impactor melt found in the bottom and walls of most craters (Kearsley et al. 2008) seem more suitable to directly determine the bulk composition of individual Wild 2 particles than of the material deposited along the tracks. The latter must recombine molten and crystalline particle remnants that are widely distributed along an entire track, in addition to a strong mixing with molten aerogel.

Qualitative elemental analysis of impactor remnants in hypervelocity craters via SEM-EDS methods is long established. It has been employed to examine a variety of space exposed surfaces, beginning with the Solar Maximum mission (e.g., Warren et al. 1989) and extending to the Long Duration Exposure Facility (e.g., Amari et al. 1991; Hörz et al. 1993) and other missions on low Earth orbits (e.g., Graham et al. 2001). Advances in instrumentation and software allow for quantitative elemental analyses of residues when the correct sample geometry can be attained (e.g., Kearsley et al. 2007b, 2008). A major breakthrough in the analysis of crater residue was accomplished recently by the manufacture of cross sections through entire micron-sized craters using focused ion beam (FIB) milling methods (Leroux et al. 2006; Graham et al. 2006). Either complete or partial crater sections may be sufficiently milled to be electron transparent and thus suitable for TEM studies, including quantitative compositional analyses of very small sample volumes via EDS techniques and phase identifications via electron diffraction. The present paper now expands these previous investigations on experimental craters, to actual Stardust impacts.

The purpose of this report is to describe the TEM observations of residues in eight individual Stardust craters that were sectioned and prepared by FIB during the Stardust Preliminary Examination. It is important to note that the suite of craters analyzed here ranges from 1.0 to 3.0 μm in lip-to-lip diameter. Based on the crater-calibration experiments by Kearsley et al. (2007b), the corresponding impactors would be either 0.25 to 0.75 μm or 0.6 to 1.5 μm in diameter, depending on their assumed density, 2.4 g/cm^3 or 0.45 g/cm^3, respectively. The initial impactor sizes of our sample suite are thus much smaller—typically by one order of magnitude—than those recovered and analysed to date from most aerogel tracks as summarized by Zolensky et al. (2006) or Flynn et al. (2006). The analytical results of the present paper refer to the smallest cometary particles analyzed via quantitative TEM to date and represent independent, but highly complementary, data to those obtained for the much larger impactors and their fragments analyzed by all other efforts of the Stardust Preliminary Examination (Kearsley et al. 2008).

SAMPLES AND METHOD

The present FIB-TEM crater studies were pursued in parallel at three different institutions: University of Lille (UL), the Naval Research Laboratory (NRL) and Lawrence Livermore National Laboratory (LLNL). After SEM/EDS investigation we selected eight craters from foils C2114N, C2068W, C2043N, C2054W, and C2100N, as described in Table 1, either on morphological or compositional criteria. From these typical examples of Stardust micron-sized craters (Fig. 1), we prepared electron transparent sections using FIB lift-out methods. FIB sample preparation is a relatively new TEM sample preparation technique, initially developed by the microelectronic industry and now used extensively for preparing TEM specimens of various geological and astrophysical materials (Heaney et al. 2001; Lee et al. 2003; Stroud et al. 2004; Zega et al. 2007). One of the main advantages of this technique is the high spatial resolution with which specific regions of interest may be isolated and prepared for detailed TEM analyses. We successfully demonstrated the method on experimental impact craters studied prior to the Stardust sample return (Graham et al. 2006; Leroux et al. 2006). Figure 2 illustrates the main steps of the FIB sample preparation process. We all used dual beam FIB tools. The initial imaging of the craters was performed by the electron beam rather the ion beam in order to prevent amorphization of the near surface. The studied residues of the craters are then free of ion beam damage. Two different protective layers have been used on the regions of interest prior to the initially high beam current milling stages of the TEM preparation procedure. Some craters (#1–4, 8) were covered by Pt before the milling process, while C-coating was used for craters #5–7. As it is likely the cometary impact residues may contain sulfide phases there is significant benefit in depositing a C layer rather than a Pt layer. As during later EDS spectral analysis, the Pt layer will produce potential spectral interference between Pt M-lines and the S K-lines. Therefore, C allows a more accurate measurement of the S content within the preserved residue. Two extraction

Table 1. Characteristics of the craters selected for the TEM studies, for which SEM images are shown in Fig. 1. Crater diameter is measured from crest to crest of the crater lip.

	Al foil, crater number	Diameter (μm)
Crater #1	C2068W, crater 6	1.40
Crater #2	C2114N, crater 1	1.26
Crater #3	C2068W, crater 12	1.65
Crater #4	C2068W, crater 11	1.53
Crater #5	C2043N, crater 1	1.82
Crater #6	C2043N, crater 2	1.45
Crater #7	C2054W, crater 13	1.05
Crater #8	C2054W, crater 11	2.95

techniques were used for the thinned samples. They include ex situ lift-out with the foil being placed onto a holey carbon film for craters #1–4, and in situ lift-out with welding of the foil onto a Cu support (crater #5–8). TEM foils are prepared in an orientation perpendicular to the sample surface and the craters are viewed in cross section under the TEM.

The UL sample preparations (craters 1–4) were performed using a FEI Strata DB 235 FIB-FESEM, which has scanning electron beam and ion beam modes. The sample FIB preparation has been done using a two stages Pt deposition for the protective layer, first assisted by electron beam in order to avoid ion beam damage and then assisted by ion beam deposition. The transfer of the electron transparent section to a TEM Cu-grid support ("lift out") was performed outside the microscope using a micromanipulator. The TEM study was performed with a Philips CM30 with a LaB6 filament operated at 300 kV and a FEI Tecnai TEM (LaB_6) operated at 200 kV. The Philips CM30 is equipped with a Thermo-Noran Energy Dispersive Spectroscopy (EDS) Si-detector with an ultra-thin window and Vantage software. The Tecnai is equipped with an EDAX EDS detector and data are processed with the FEI-TIA software. Sample thickness and element-specific yields (*k*-factor) corrections were applied to obtain quantitative elemental compositions. Laboratory *k*-factors were experimentally determined using the parameterless method of Van Cappellen (1990) with silicate standards. For silicates, specimen thickness determination for the absorption correction procedure was based on the principle of electroneutrality (Van Cappellen and Doukhan 1994). For the metal and sulfide components, the thickness was fixed to 100 nm, which is an accurate estimate for the FIB sections.

Sample preparation for the NRL studies (craters 5 and 6) were performed using a FEI Nova 600 Dual-Beam FIB-FESEM with Ascend Extreme Access lift-out tool. The craters were protected from ion beam damage by a protective carbon mask that was deposited in the FIB using the electron beam. The lift-out cross-sections were supported on Cu microtweezers, as described in Zega et al. (2007). The TEM study was performed with a 200 kV JEOL 2200FS field-emission TEM, which is equipped with a high-angle annular dark-field (HAADF) detector and a Thermo Noran System Six EDS system. At NRL, the compositions of the residue components in craters 5 and 6 were determined from both STEM-based spectrum imaging and TEM-based spot analysis measurements. For each crater, a 256 × 256 pixel spectrum image was acquired with a nominal probe size of 1 nm, at an image resolution corresponding to ~4 nm/pixel. The acquisition time was 90 min during which automated drift-compensation was applied at one minute intervals. Multivariate statistical analysis of the spectrum images, using both the Noran Compass package and Axsia (Kotula and Keenan 2006; Kotula et al. 2003) was used to determine the number of residue components, the compositions of the components, and their spatial distribution. The components determined with this statistical method comprise a basis set, so that each point in the spectral image is a linear combination of the component

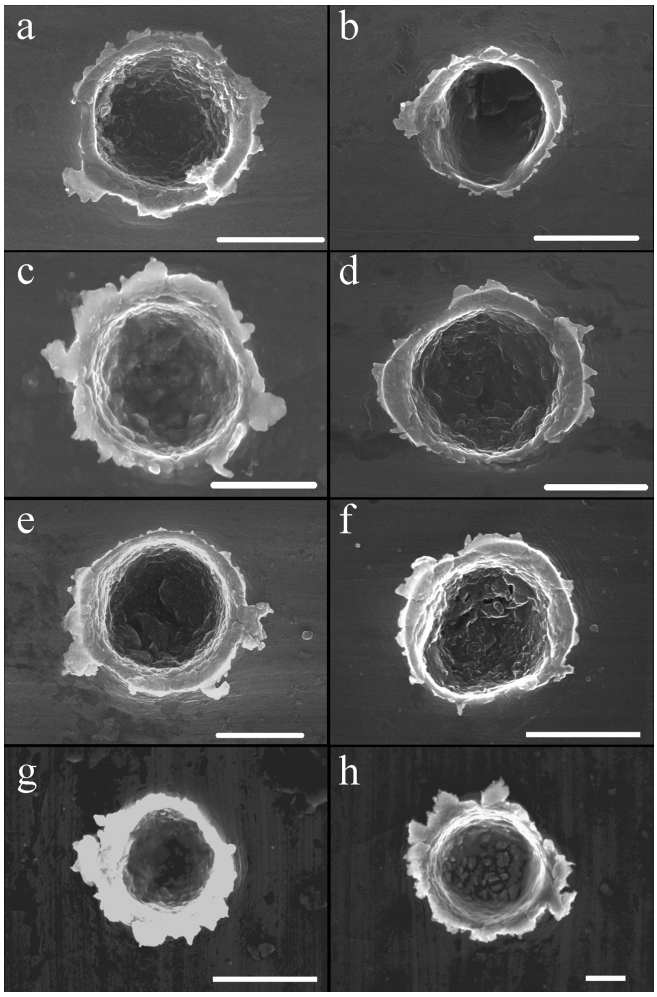

Fig. 1. Secondary electron SEM images of the craters selected for the TEM studies. Scale bar = 1 μm. a) Crater #1, C2068W. b) Crater #2, C2114W. c) Crater #3, C2068W. d) Crater # 4, C2068W. e) Crater #5, C2043N. f) Crater # 6, C2043N. g) Crater #7, C2054W. h) Crater #8, C2054W.

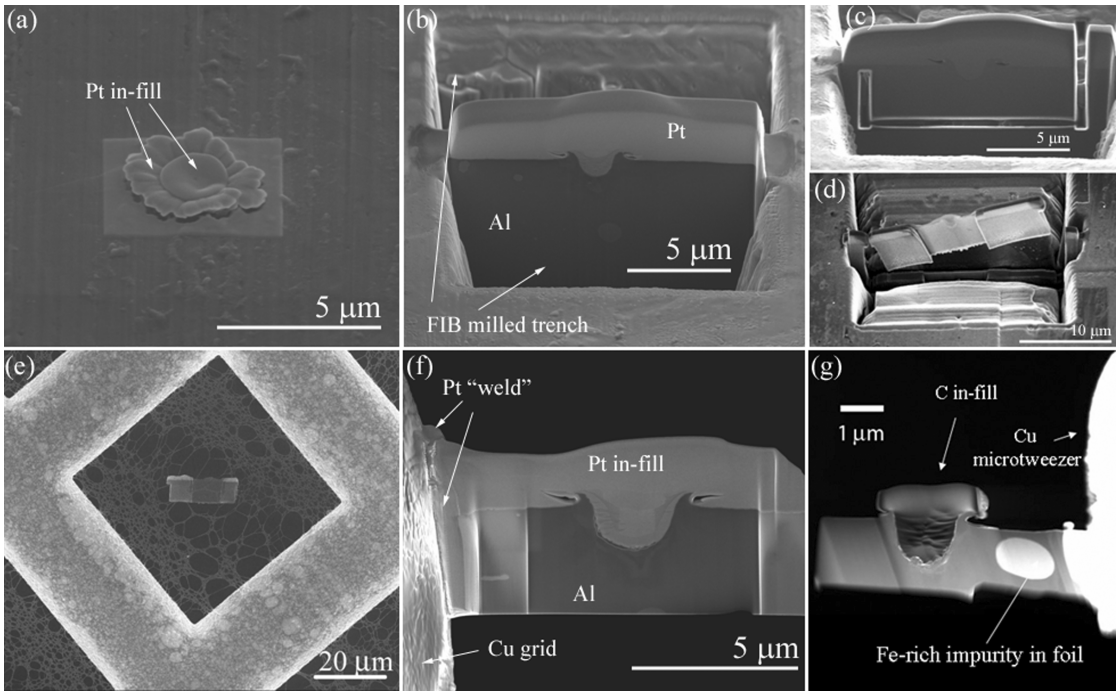

Fig. 2. Basic steps of the FIB sample preparation method. The illustrations come from different crater preparations. Illustrations (d–e) are from the ex situ lift-out and (f–g) from the welding technique. a) 5 kV secondary electron image of crater #8 after the deposition of the Pt layer with ion beam assisted chemical deposition to protect the residue lining the wall and base of the crater during the FIB milling process. b) 5 kV secondary electron image of the crater #8 after the initial FIB milling has produced trenches on either side of the region of interest. At this stage the FIB milling uses a convergent, intense beam of 30 keV Ga^+ ions (current typically 20 nA). The cross-sectional profile of the crater is clearly visible in the image. c) 30 kV ion-induced secondary electron image of the cross sectional slice after it has been thinned to approximately 1 µm. The sections prepared using the FIB technique varied slightly between the three institutions due to different extraction methodologies. At LLNL and NRL the sections were extracted from the bulk foils in situ (in chamber micro-manipulators) whereas the University of Lille utilized an exo-lift-out approach using micro-manipulators attached to an optical microscope. For in situ extraction of the section using the technique described in Graham et al. (2006), side-wall cuts and an under-cut are made into the section to enable lift-out. d) For the exo-lift-out extraction the crater (#3) cross section has been thinned to electron transparency while still in the foil substrate. The final stage of sample thinning is performed by a progressively decrease of the ion-beam current (up to 50 pA). FIB has then been used to cut the thin-section free ready for lift-out (Leroux et al. 2006). e) TEM bright field image of the exo-lift-out FIB section after it has been deposited on a carbon film supported by a Cu TEM grid. f) 5 kV secondary electron image of the in situ lift-out crater section shown in images (a–c) after it has been attached to a TEM grid and thinned to electron transparency (LLNL methodology). g) 200 kV STEM dark field image of a crater section extracted using the in situ method described in Zega et al. (2007). The crater (#5) in this image has been filled with C instead of Pt which allows a more accurate measurement of the S content within the preserved residue, as it avoids possible peak overlap between Pt and S.

spectra. The advantages of this technique are that it provides a statistically robust analysis of correlations in the spatial distribution of the identified elements, i.e., all phases present, including interface reactions, are readily identified, and because full spectra are retained, quantitative analysis of the maps can be performed. The component spectra were quantified using Cliff-Lorimer routines with thickness absorption corrections and library *k*-factors. The counting statistics permit very precise analysis (<0.1 at%), however the actual uncertainty in the accuracy of compositions is limited by the uncertainty in sample thickness and overlap of the phases in the thickness of the sample, and is estimated at ±3 atom%.

The focused ion beam work at Lawrence Livermore National Laboratory (crater 7–8) was performed using an FEI Nova 600 Nanolab DualBeamTM focused ion beam (FIB)/ field emission gun scanning electron microscope (SEM) fitted with an EDAX Genesis X-ray energy dispersive spectrometer (EDS). The sections were extracted using an Ascend micro-manipulator system. To protect the impact residue during the ion milling procedure a Pt "plug" was deposited in the interior of the crater using 5 kV electron beam assisted chemical deposition. The entire crater was then capped with a Pt "strap" using 30 kV ion beam assisted chemical deposition. The ion beam (FIB) was used to trench either side of the Pt "strap" to produce a cross-sectional profile of the sample. The section containing the cross-sectional profile was then thinned to approximately 1 µm thickness after which the ion beam was used on the side wall and under cuts to enable the section to be extracted from the bulk foil. The section was extracted from the bulk foil and attached to a TEM grid. The section

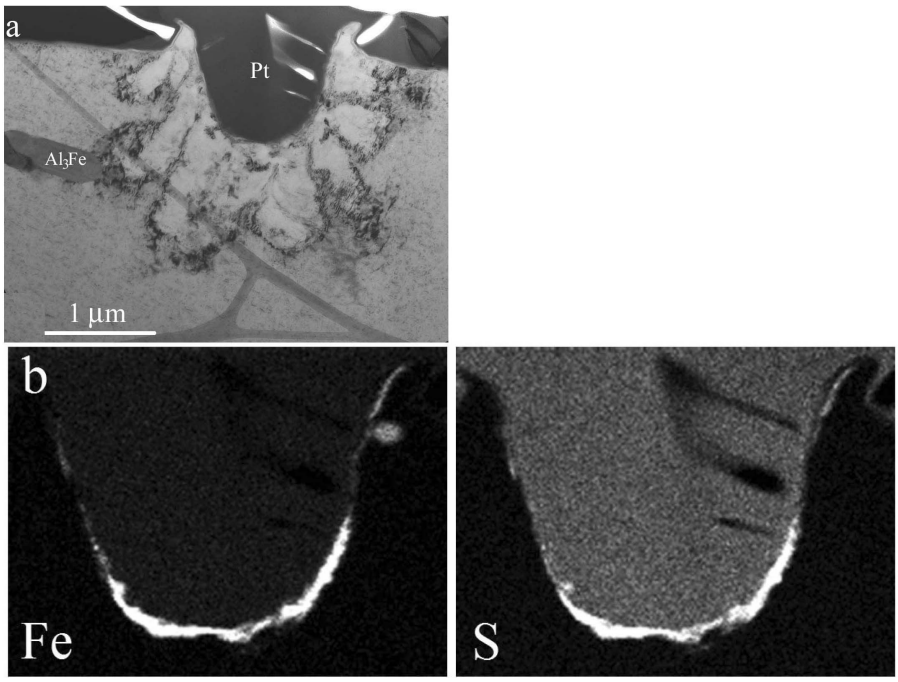

Fig. 3. a) Bright-field TEM image of crater #1. Note the deformation features in aluminium, below the crater, visible by the Bragg contrast. Note also the presence of an Al_3Fe inclusion. b) EDS intensity maps for Fe and S. Note the excellent correlation between the two elements. The only other detectable element was Ni, present in low concentration.

was then subjected to further low beam current milling to thin to electron transparency (80–100 nm thick). The TEM study was done using a 200 kV field emission FEI Tecnai G2 F20 with an EDAX EDS and FEI-TIA processing software. For microanalysis data reduction the Cliff-Lorimer method with stored *k*-factors was employed. The accuracy of the method was assessed by analyses of thin-film glass standard (NIST-SRM2063) and crystalline silicates (e.g., forsterite) in the craters. In crater #7, reported major element abundances are accurate to within ±3 at%. In crater #8, where Pt rather than C was used as a capping layer (Fig. 10), line-of-sight X-ray absorption precluded quantification especially for light elements like oxygen. Reported element abundances for crater #8 are semi-quantitative at best.

RESULTS

All of the cross-sectional TEM samples show deformation of aluminium underneath the crater floor (Fig. 3a). Numerous dislocations have been generated, and extend from the crater walls mainly in the form of dislocation cells. Aluminium in contact with the residue is frequently recrystallized, suggesting a combination of plastic deformation and heating due to the impact. This recrystallized layer, when present, does not exceed 0.3 µm. These features (generation of dislocations and recrystallization) are typical for hypervelocity impacts in metallic targets (e.g., Ferreyra et al. 1997; Murr et al. 1998; Leroux et al. 2006). We have also seen some Fe-rich inclusions in the aluminium targets (Fig. 3a). Their presence in Stardust Al foils has been already reported by Kearsley et al. (2006) and Leroux et al. (2006). EDS measurements performed on a few of them showed that they are precipitates close to the Al_3Fe stoichiometry, with minor Ni (0.4 at%). These inclusions do not cause problems for the present residue studies by TEM, but they could be a source of error for SEM-based EDS analysis. Future SEM and TEM studies should account for the possibility of a cometary grain impacting directly on such an inclusion, leading to contamination of the residue with terrestrial Fe.

Crater #1

The amount of residue in this crater (Fig. 3a) is low and located mainly on the crater floor, while almost completely absent on the walls. The thickness of the residue layer is irregular and <50 nm. EDS elemental distribution maps show that it contains only Fe, S, and minor Ni, with a good correlation between the three elements (Fig. 3b). Quantitative EDS measurements yield Fe:S atomic ratios ranging from 46:53 to 58:41 (Table 2 for representative compositions). The average ratio is 51:48 based on 17 analyses that covered the entire residue. The average Ni concentration is 0.9 at%. These compositions suggest that the impactor was a single grain of pyrrhotite, and that minor loss of S occurred during the impact.

Table 2. Representative compositions (at%) for the metal–sulfide components in the residues measured by EDS in the studied craters. Error estimates are given in brackets (1σ standard deviation).

Fe	S	Ni
Crater #1, shown in Fig. 3		
49.3 (0.6)	50.0 (0.4)	0.7 (0.1)
49.2 (0.7)	50.4 (0.5)	0.4 (0.1)
50.6 (0.6)	48.6 (0.5)	0.7 (0.1)
54.9 (0.9)	44.4 (0.6)	0.7 (0.1)
Crater #3, shown in Fig. 5		
87.5 (1.6)	10.4 (0.5)	2.1 (0.4)
79.5 (1.0)	16.9 (0.3)	3.6 (0.3)
72.8 (1.1)	26.0 (0.5)	1.1 (0.2)
59.2 (0.8)	40.0 (0.5)	0.8 (0.2)
Crater #4, shown in Fig. 6		
86.4 (1.9)	7.4 (0.5)	6.2 (0.6)
74.7 (2.2)	21.8 (0.9)	3.5 (0.7)
59.5 (2.4)	39.4 (1.4)	1.1 (0.5)
45.6 (2.0)	53.3 (1.6)	1.1 (0.4)
Crater #5, shown in Fig.7		
74.2 (0.6)	15.7 (0.6)	10.1 (0.4)
Crater #6, shown in Fig. 8		
79.4 (0.4)	18.9 (0.4)	1.7 (0.1)

Crater #2

This crater has a very irregular morphology. As shown in Fig. 4a the residue is unusual as it is not a continuous melt-liner draping the crater bottom, but a single grain implanted in the Al with no evidence of internal flow, indicating that the particle escaped melting. The particle has a fairly rectangular shape, 500 × 250 nm in size, and its edges are rounded. Bright-field images display diffraction contrast showing that the particle was crystalline (Fig. 4b) but it appeared unstable under the electron beam. Unfortunately, the electron beam rendered it almost fully amorphous before the acquisition of any electron diffraction pattern. Only very small domains remained crystalline and stable under the electron beam and their diffraction patterns are compatible with both clino-enstatite and ortho-enstatite (Fig. 4c). The EDS mapping and quantitative spectra show that the composition is homogeneous across the whole grain, and very close to stoichiometric enstatite ($MgSiO_3$; see Table 3). The concentration of minor elements is compatible with a pyroxene.

Crater #3

The residue is abundant, mainly lining the crater floor, but it is very thin in the lateral walls; the residue thickness reaching a maximum of 200 nm in one region. Figure 5a shows a general view of the crater, taken in the STEM mode. The accompanying TEM bright-field image

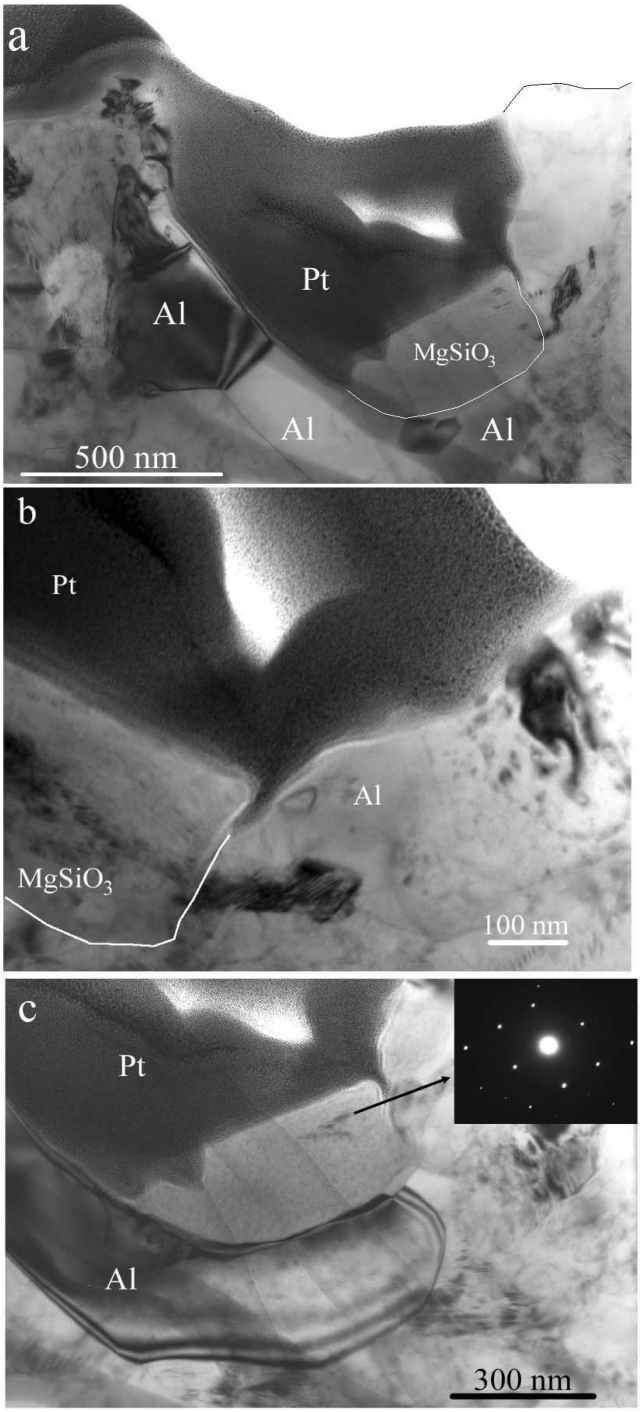

Fig. 4. Bright-field TEM images of crater #2. a) General view showing the irregular shape of the crater, with a large $MgSiO_3$ particle implanted at its base. The contact of the particle with the aluminium is indicated by white line. b) Magnified view showing that the particle displays Bragg contrast, and thus was crystalline, but unstable under the electron beam. c) Implanted particle after the EDS mapping. A crystalline remnant is oriented in diffraction Bragg condition. The corresponding selected area electron diffraction is shown in the insert, compatible with both clino (zone axis [2,1,2]) and orthopyroxene (zone axis [−1,1,1]).

Table 3. Representative compositions (at%) for silicates present in the crater residues measured by EDS. Error estimates are given in brackets (1σ standard deviation); nd = not detected.

O	Si	Mg	Fe	Ca	Cr	Mn	Remarks
Crater #2, shown in Fig. 4							
60.0 (0.7)	20.0 (0.5)	19.0 (0.6)	0.28 (0.03)	0.19 (0.04)	0.33 (0.04)	0.09 (0.03)	Enstatite
Crater #3, shown on Fig. 5							
57.8 (0.7)	14.5 (0.4)	26.1 (0.5)	1.4 (0.1)	0.10 (0.03)	nd	0.18 (004)	Olivine Fo_{95}
56.9 (1.0)	13.7 (0.5)	26.9 (0.6)	2.2 (0.2)	0.21 (0.05)	nd	0.15 (0.04)	Olivine Fo_{92}
57.6 (0.9)	15.0 (0.4)	25.7 (0.5)	1.8 (0.2)	0.03 (0.01)	0.02 (0.01)	0.02 (0.01)	Olivine Fo_{93}
61.4 (1.4)	22.8 (0.7)	15.5 (0.7)	0.26 (0.07)	nd	nd	nd	Amorphous
60.1 (1.7)	20.2 (0.8)	17.6 (0.8)	1.7 (0.3)	0.25 (0.08)	0.02 (0.01)	0.11 (0.06)	Amorphous
59.6 (1.0)	19.3 (0.5)	17.9 (0.5)	2.6 (0.2)	0.23 (0.05)	0.13 (0.03)	0.10 (0.04)	Amorphous
Crater #4, shown in Fig. 6							
60.5 (1.3)	20.0 (0.5)	8.9 (0.4)	4.1 (0.3)	4.1 (0.3)	2.2 (0.2)	0.20 (0.08)	Pyroxene
57.9 (0.7)	16.0 (0.4)	22.0 (0.5)	3.4 (0.2)	0.4 (0.1)	nd	0.13 (0.05)	Olivine Fo_{86}
59.9 (1.1)	19.8 (0.5)	17.2 (0.6)	1.4 (0.2)	1.5 (0.2)	0.15 (0.04)	nd	Amorphous
60.6 (0.6)	21.2 (0.3)	15.4 (0.3)	1.5 (0.1)	0.9 (0.1)	0.12 (0.03)	0.19 (0.06)	Amorphous
59.9 (0.8)	19.9 (0.4)	12.6 (0.3)	5.1 (0.2)	1.8 (0.1)	0.34 (0.06)	0.23 (0.07)	Amorphous
Crater #5, shown in Fig. 7							
57.1 (0.3)	14.3 (0.1)	28.4 (0.1)	nd	0.05 (0.01)	0.02 (0.01)	0.08 (0.01)	Forsterite
57.4 (1.1)	14.6 (0.2)	28.0 (0.4)	nd	nd	nd	nd	Forsterite
Crater #6, shown in Fig. 8 (1σ)							
57.0 (0.4)	13.6 (0.1)	28.6 (0.1)	0.06 (0.01)	nd	nd	0.05 (0.01)	Forsterite
Crater #7, shown in Fig. 9							
59.3 (0.4)	18.6 (0.2)	14.8 (0.2)	5.8 (0.4)	1.2 (0.1)	0.13 (0.03)	0.30 (0.04)	Amorphous
58.8 (0.2)	17.5 (0.2)	14.9 (0.1)	7.4 (0.2)	0.96 (0.04)	0.33 (0.03)	0.08 (0.02)	Amorphous
58.8 (0.4)	17.5 (0.2)	17.6 (0.2)	4.6 (0.4)	1.3 (0.1)	nd	0.22 (0.04)	Amorphous
58.1 (0.3)	16.2 (0.2)	18.2 (0.2)	5.8 (0.2)	1.4 (0.1)	0.18 (0.03)	0.10 (0.03)	Amorphous
58.2 (0.3)	16.3 (0.3)	21.7 (0.4)	2.3 (0.3)	1.1 (0.1)	0.21 (0.05)	0.24 (0.05)	Amorphous
Crater #8, shown in Fig. 10							
57.7 (0.4)	15.0 (0.2)	22.6 (0.3)	4.6 (0.2)	0.12 (0.02)	0.08 (0.02)	0.18 (0.03)	Olivine Fo_{83}
57.4 (0.5)	15.9 (0.3)	22.5 (0.3)	4.7 (0.2)	nd	nd	0.22 (0.05)	Olivine Fo_{83}
57.1 (0.5)	14.3 (0.2)	23.9 (0.3)	4.6 (0.2)	nd	nd	0.11 (0.04)	Olivine Fo_{83}
58.1 (0.4)	16.2 (0.3)	20.1 (0.3)	5.1 (0.3)	0.14 (0.02)	nd	0.25 (0.05)	Olivine + amorphous
58.9 (0.6)	17.2 (0.5)	17.3 (0.4)	6.6 (0.5)	0.63 (0.10)	nd	nd	Amorphous
56.8 (0.6)	13.5 (0.5)	21.1 (0.4)	7.9 (0.4)	nd	0.33 (0.06)	0.33 (0.07)	Amorphous

(Fig. 5b) shows that numerous crystallites, typically 50 nm size, are present in the residue. The residue is mainly crystalline and all diffraction patterns are compatible with olivine. Most of the grains are irregularly shaped, with a relative disorientation of a few degrees for adjacent grains. They are thus probably subgrains, separated by planar defects. EDS analysis has confirmed that the crystals are olivine, with forsterite content ranging from Fo_{91} to Fo_{95}. Representative compositions are given in Table 3. Close to the top side of the residue, two small amorphous pockets have a composition close to pyroxene (Mg + Fe/Si ~ 1). We have not found any crystalline material in these two regions. Sulfur and iron are found mostly on one side of the crater, located at the residue/aluminium interface, and mixed with a SiO_2-rich silicate component. Fe does not always correlate with S, and in general Ni and S are anticorrelated suggesting the coexistence of Fe,Ni metal and Fe sulfides (see Discussion section). Due to the very fine scale of intermixing, it was not possible to extract exact phase compositions due to overlap in the thickness of the TEM section. The Fe:S atomic ratio ranges from 90:10 to 60:40 (see Table 2 for representative compositions). The average composition (on 17 analyses) is Fe:S:Ni = 72.6:25.5:1.9 at%. At one edge of the residue, there is evidence for melt flow (Fig. 5c), consisting of a mixture of metal (with a low concentration of S) and a SiO_2-rich component with an atomic ratio of Si to the other cations at ~4/1.

Crater #4

Again the residue on the crater floor is abundant and is of irregular thickness, from 30 to 150 nm. Figure 6a shows a general view of the crater. Several crystallites are present in the residue. Most of them are very small with the largest

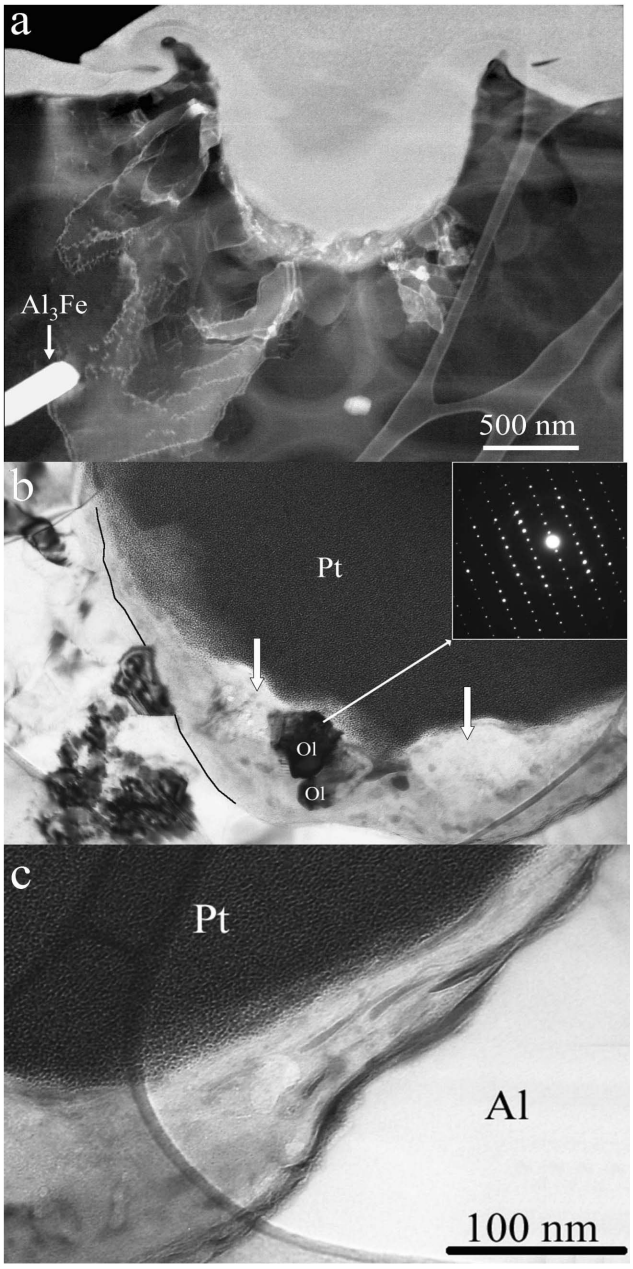

Fig. 5. a) Dark-field STEM image showing a general view of crater #3. Plastic deformation of aluminium is evidenced by the presence of dislocations, most of them being reorganized into subgrain boundaries. Note the presence of an Al_3Fe precipitate. b) Bright-field TEM image of the residue. Two large olivine (Ol) crystallites ($Fo_{92–93}$), with a slight misorientation of a few degrees, are oriented along the [001] zone axis. The corresponding SAED is shown in the insert. Other crystalline grains are also present but are not visible here because they do not diffract at this specific foil orientation. At each side of these the crystallites amorphous pockets are present (brighter areas, arrowed) for which composition is close to pyroxene. The contact of the residue with aluminium is marked by a dark line to better visualize the residue outline. c) Bright-field TEM image showing flow structure of a mixture of Fe-S (elongated darker regions) and SiO_2-rich material observed at the right edge of the residue deposit.

approximately 100 nm in size. Two crystallites have been studied by selected area electron diffraction (SAED); both are consistent with clinopyroxene (C2/c space group). EDS elemental distribution revealed a complex chemistry for the entire residue (Fig. 6b). Regions rich in Ca are well correlated with large pyroxene grains as shown on Fig. 6a. Quantitative analysis revealed that the pyroxene grains are Ca and Cr-rich (Table 2). Due to their small size and the unavoidable overlap with the matrix within the volume of the 100 nm thick TEM section, we were unable to extract their exact composition. Interestingly, the Mg-rich areas, which have a composition close to olivine, seem mainly amorphous. Only one small olivine crystallite has been found and analyzed. The amorphous material, which contains the majority of the residue, is highly variable in composition from point to point (Fig. 6b; Table 3). There is no systematic correlation between Mg, Si, and Ca, suggesting the presence of a complex assemblage containing amorphous material and crystallites of variable compositions. The Si/cation ratio, measured in areas where S is absent, is close to 1, meaning that the melt probably originated from a pyroxene-dominated assemblage. Fe- and S-rich regions form thin discontinuous layers both at contacts of the residue with aluminium and the residue with free surface (Fig. 6b). Fe and S are not always correlated, suggesting that Fe is present as metal (see Table 2 for representative compositions). Compositions extend from Fe:S:Ni = 46:53:1 (pyrrhotite) to 87:7:6. In summary, the residue is dominated by pyroxene components, with minor olivine, metal, and sulfide.

Crater #5

STEM-based EDS spectral imaging with multivariate statistical analysis (MSA) and HAADF imaging (Fig. 7) demonstrate that this residue consists of two compositionally distinct components. The dominant component is ~200 nm thick and has the composition of forsterite with trace Ca, Cr, and Mn (Fig. 7a; Table 3). The second component is ~10 nm thick with a Fe,Ni-sulfide composition that is very depleted in S, e.g., Fe + Ni/S = 6. Trace S and Fe appear in the silicate spectra, and small Mg and Si peaks appear in the sulfide spectra, because there are some regions in which the two phases overlap in the thickness of the TEM section. This does not hinder the quantification of the spectra, because of the immiscible nature of these two components. All features of the spectrum images result from a combination of the two residue components, the Al foil, FIB-deposited carbon mask, the Cu sample support, plus noise. No other spatially or compositionally distinct components, such metal, oxides, or other silicate phases are observed in the spectral image data or HAADF images. However, very fine-scale components, i.e., ~2 nm, could go undetected because the EDS measurements and HAADF

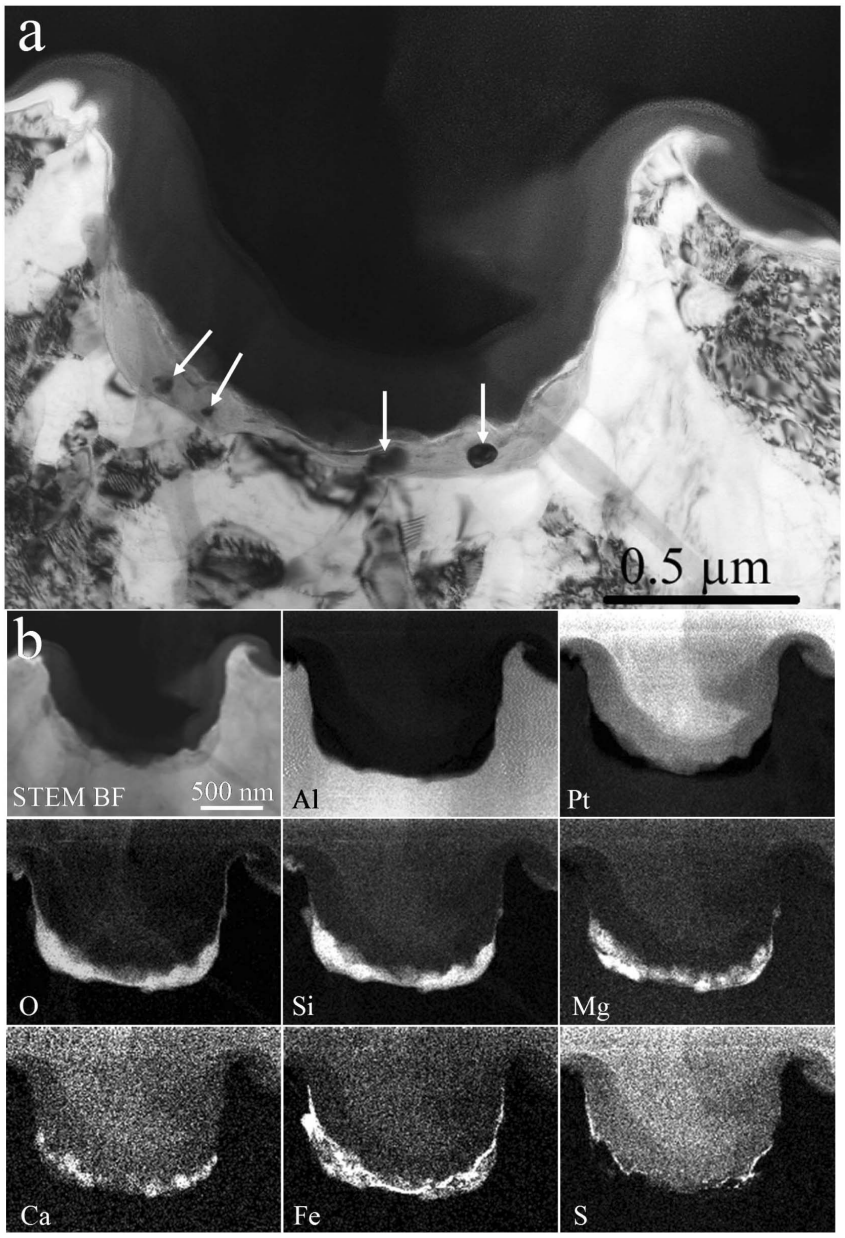

Fig. 6. a) Bright-field TEM image of crater #4. Note the presence of numerous crystallites in the amorphous matrix (arrowed). One of them is in strong diffraction orientation. b) EDS Elemental distribution maps for Al, Pt, O, Si, Mg, Ca, Fe, and S. Note that the elemental distribution is highly heterogeneous.

contrast derive from the full thickness of the section (~150 nm).

The sulfide component wets both the crater wall and the forsteritic component, indicative of complete melting. The forsteritic component appears to wet the right side of the crater wall, consistent with significant melting, but appears as a distinct grain on the lower left side (Fig. 7c, white box). Bright field imaging (Figs. 8a and 8b) confirms that the metal-sulfide coats the crater surface and silicate residue as a result of melting. Under equilibrium conditions, material with this composition would crystallize into separate metal and sulfide components, however there is no direct evidence for phase separation in this particular residue. One possible explanation is that the phase separation is present at too fine a scale to be observed by HAADF imaging or in the multivariate statistical analysis.

The crystallinity of the largest grain with forsterite composition is confirmed by selected area electron diffraction (Fig. 8b, inset). The SAED spots show some streaking into arcs, consistent with a spread in the grain orientation. Dark-field imaging (Figs. 8c and 8d) reveals distinct domains, slightly tilted from each other. This

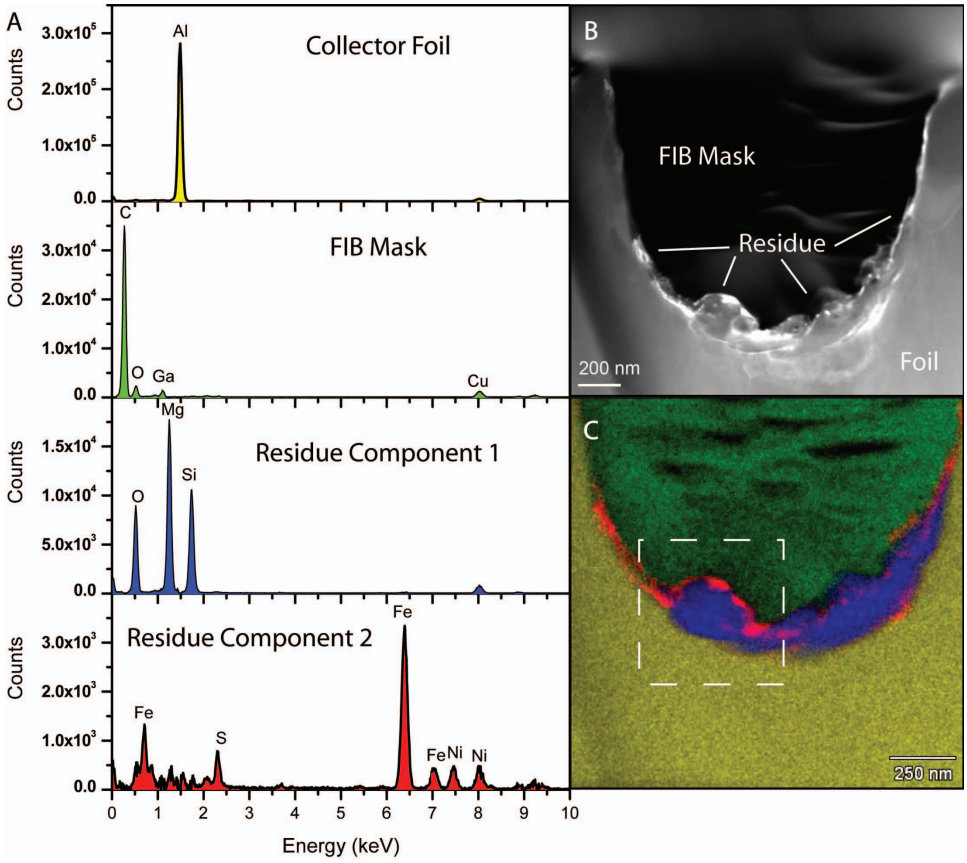

Fig. 7. a) Four principle component spectra obtained from the multivariate statistical analysis (MSA) of EDS spectrum imaging of crater #5. The MSA shows that there are two spatially distinct residue components: a silicate with a forsteritic composition and an Fe-Ni sulfide, in addition to the Al collector foil and the FIB-deposited carbon mask. The Cu peaks result from the sample support. All features in the spectrum images are a combination for these four components, plus noise. No additional spatially or compositionally distinct residue components, such as metal, oxide or other silicate phases, were found. b) High-angle annular dark-field image. The sulfide residue appears bright, and the silicate dark due to the Z dependence of the contrast. c) Composite principle component map: silicate (blue), sulfide (red), Al foil (yellow), and FIB-deposited carbon (green): The white outlined box indicates the portion of the residue on which diffraction studies were performed, as illustrated in Fig. 8.

small spread in orientation is consistent with shock-induced alteration of crystalline material, rather than crystallization from a melt.

These results indicate that this crater was produced by the impact of one or more ~200 nm scale forsterite grains associated with metal and sulfides. The largest silicate grain appears to be minimally altered by shock, mostly retaining its original composition and crystallinity.

Crater #6

This residue is concentrated in the floor of the crater, but extends up one sidewall, with a thickness variation from 10 to 250 nm (Fig. 9). The individual residue grains are difficult to distinguish by bright-field TEM imaging (not shown), but HAADF imaging (Fig. 9b) and MSA of EDS analysis (Figs. 9c and 9d) show that the residue consists of a 10 to 25 nm-scale mixture of forsterite and Fe,Ni sulfide grains. The sulfide is depleted in sulfur, with (Fe + Ni)/S = 5.9, implying the presence of separate metal and sulfide phases, however there is no direct evidence for such phase separation and, alternatively, some S may have been lost upon impact. The thickness of the TEM section and the fine-grained nature of the residue prevented diffraction analysis to assess the crystallinity of either component. The impacting particle in this case likely consisted of 10 nm scale metal sulfides and 100 nm scale olivines, but little, if any, primary grain structure is retained.

Crater #7

The residue is thin (typically 30 nm), continuous and is present also on the crater's lateral walls (Fig. 10a). A very large number of crystallites are present, but are too small to be identified. Elemental distribution (Fig. 10b) and quantitative EDS measurements show that the residue consists of a mixture of silicates and sulfides. Mg, Si, and O seem mainly present on the crater floor while Fe and S occur

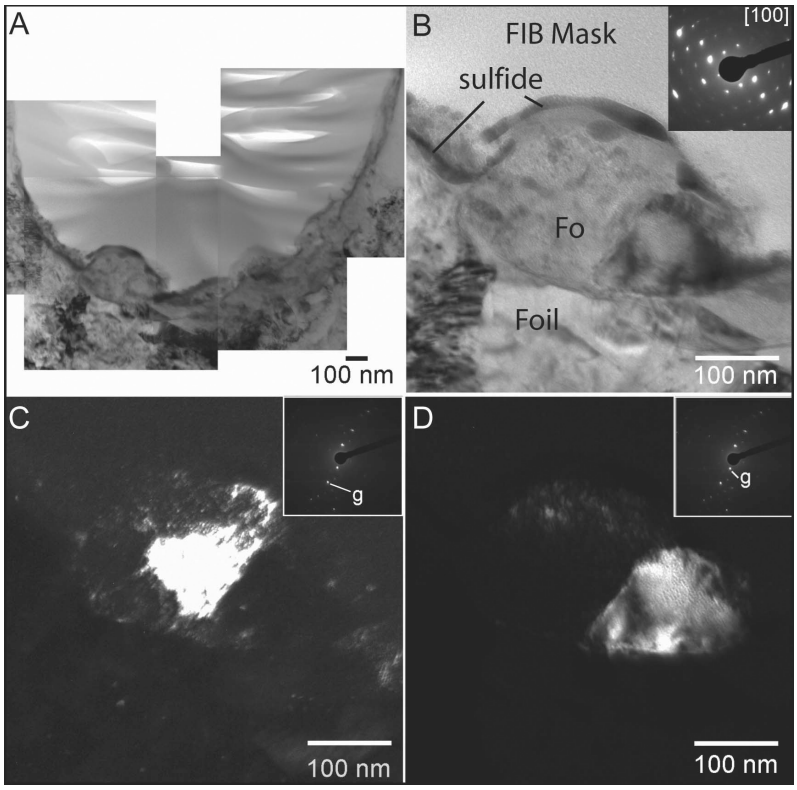

Fig. 8. a) Bright-field TEM of crater #5. b) Bright-field TEM image and SAED (insert) a forsterite grain from the left side of the crater. c) and d) Dark-field TEM images of the forsterite grain illuminating the slight orientation variation between the grain center (g = 0,–6,–2) and bottom right (g = 0,–2,–1), respectively.

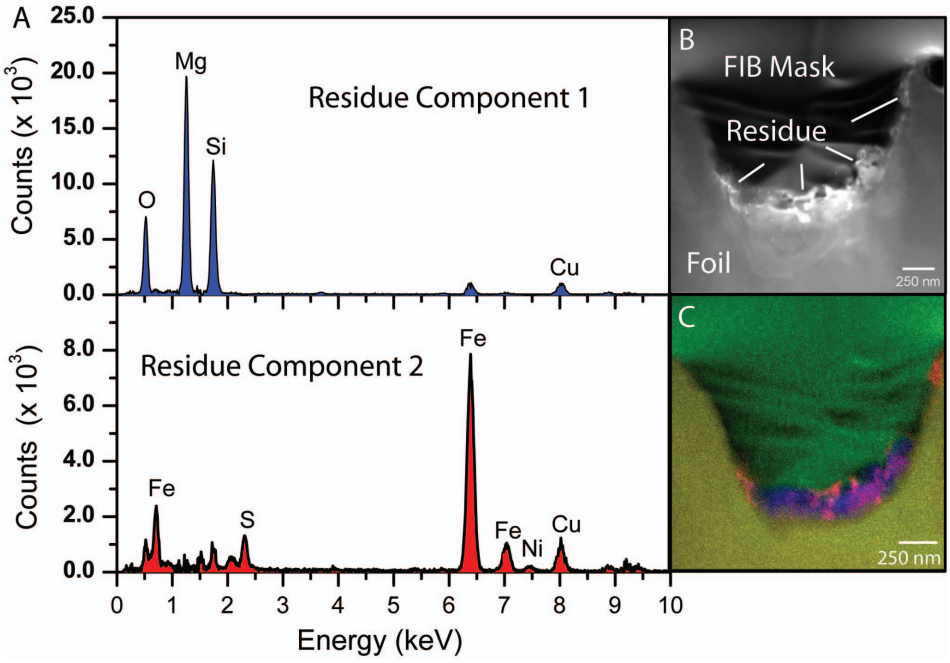

Fig. 9. a) EDS spectra from the two cometary residue components in crater #6, identified by MSA. The Mg-rich silicate (blue) and Fe-Ni sulfide (red) components were the only spatially and compositionally distinct components in the spectrum images other than the Al foil and carbon mask. b) High-angle annular dark-field image. The sulfide (bright) is interspersed with the silicate (dark) a residue at a scale of ~10 nm. c) Composite principle component map showing the two residue components: silicate (blue) and sulfide (red), in addition to the Al foil (yellow) and FIB-deposited carbon mask (green).

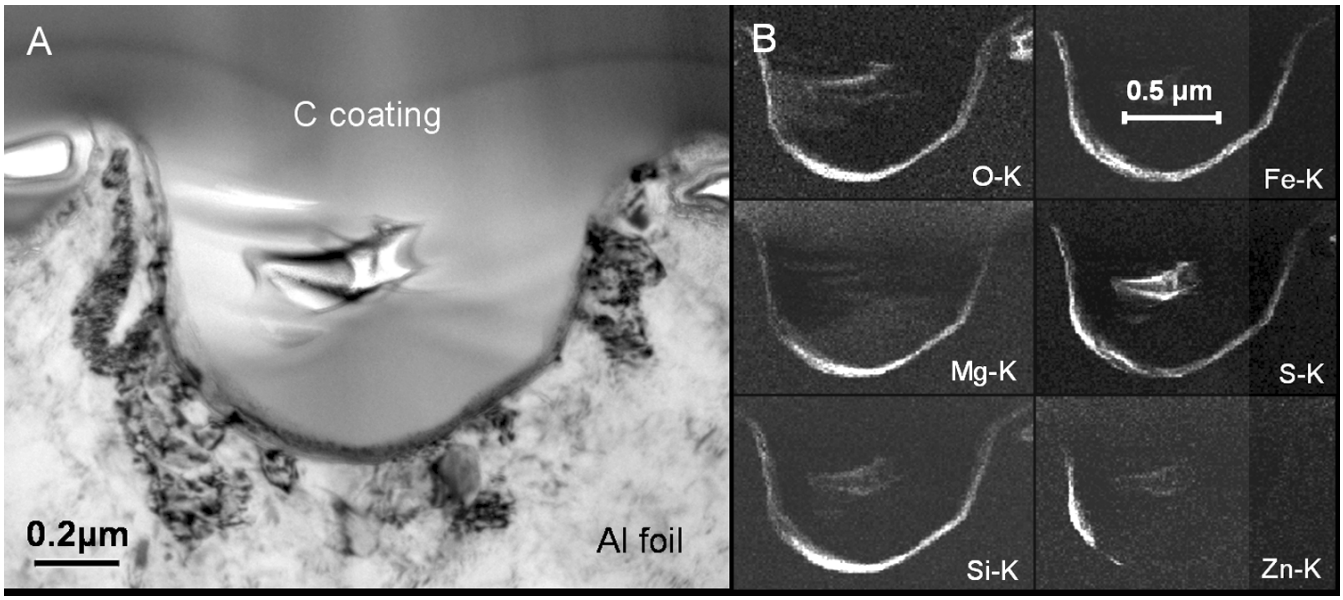

Fig. 10. a) Bright-field TEM image of crater #7. b) X-ray EDS maps showing elemental distribution for O, Si, Mg, Fe, S, and Zn over the residue.

mostly on the lateral wall. Assuming the 1:1 stoichiometry for the Fe-S component, we deduced an estimate of the silicate stoichiometry. The ratio Si/cations is found to vary between 1 and 2, suggesting a mixture of olivine and pyroxene. The presence of Ca also suggests the presence of pyroxene in the incident particle. Recalculated estimation of the composition is given in Table 2. The residue also contains a significant amount of Ni (average of 1 at%).

On one side of the crater, a Zn-rich region is present. The distribution of Zn correlates well with that of S, suggesting that the incident particle contained a Zn-Fe sulfide (see Zolensky et al. 2006). It is also possible that the zinc is a contaminant from the aluminium foil. Although the reported concentration of Zn within Stardust foil is very low (~75 ppm; Kearsley et al. 2007b), it is not known whether it is dispersed as a trace throughout, or as rare, discrete, Zn-rich inclusions.

Crater #8

The residue layer within this crater is highly variable in thickness (up to 200 nm) with the most abundant material lining one side of the crater wall (Fig. 11a). The dark field imaging reveals that the amorphous layer contains numerous nanometer sized crystallites (Figs. 11b and 11c) with HRTEM confirming these to be olivine (Fig. 11d). EDS elemental distribution maps shows that the residue is very homogeneous in composition. Quantitative EDS show that crystals and the amorphous matter have the same composition, very close to the olivine stoichiometry, with Fo content = 83. These TEM observations would strongly imply that the original cometary impactor was a single mineral phase.

DISCUSSION

Dominant Mineralogy of the Residues

The main characteristic of the residues in the 8 small (<3 um) craters analyzed to date is their large diversity, as is also noted in the SEM-EDS studies of a large population of small craters, reported by Kearsley et al. (2008). Their projectiles, all <1 µm in diameter, seem dominated volumetrically by a limited number of phases. These small scale residues differ strongly from those in large (>50 µm) Stardust craters which commonly consist of polymineralic melt with a chondritic-like composition (Flynn et al. 2006; Kearsley et al. 2008). The composition of the small crater residues does not correspond to chondritic melts. These differences are probably due to the fact that small craters were sampling closer to the smallest individual mineral grains of Wild 2 material, whereas the larger craters averaged more thoroughly over the modal abundance of Wild 2 minerals and their sizes. Nevertheless, crater morphology and residue composition suggest that the majority of impactors <1 µm are still made up of polymineralic materials. Table 3 summarizes the mineralogy we deduce from the observations. We have also included in the table a rough estimate of the modal phase proportions. Three of the craters originated from monomineralic projectiles, which are Fe sulfide, $MgSiO_3$ pyroxene and olivine (Fo_{83}) for crater #1, 2, and 8, respectively. Crater #4 is substantially dominated by pyroxenes, and craters #3, 5, and 6 are dominated by olivine, with Fo contents of 93, 100, and 99.5, respectively. Crater #7 seems the most complex because the silicate stoichiometry suggests a mixture of olivine and pyroxene, in association with Fe and Zn-Fe sulfides.

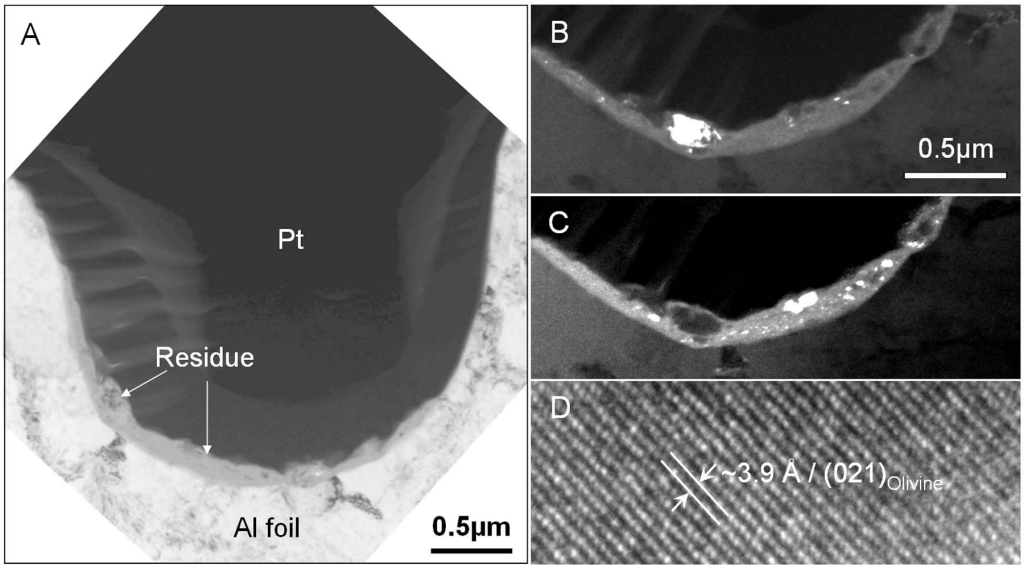

Fig. 11. a) Bright-field TEM image of crater #8. b) and c) Dark-field TEM images of a part of the crater, which were taken by using different operating reflections. Crystalline grains that are diffracting electrons are illuminated (i.e., white on the image). d) HRTEM image of the bigger crystallite displaying a bright contrast in (b).

What Were the Original Densities of the Dust Impactors?

Kearsley et al. (2006, 2007b) conducted impact experiments into Stardust foils at 6 km/s to determine the relationship of crater diameter and depth to impactor diameter and density. The crater depth/diameter (D_p/D_c) ratio was found to be strongly dependant on the impactor density for a suite of non-porous projectiles that included stainless steels (D_p/D_c = 0.85), pyrrhotite (0.65), olivine (0.65), pyroxene (0.61), soda-lime glass (0.53), and polymer polymethylmethacrylate (0.42). Recent experiments also show that particle shape and aspect upon impact can be important in controlling D_p/D_c (Kearsley et al. 2008), and lead to wider ranges of D_p/D_c for natural, irregular particle shapes than are seen for spherical impactors. However, the ratios we measured on the eight Stardust TEM cross sections (Table 4) are almost all significantly lower than might be expected for the original mineralogy deduced from the residue compositions. The only exception is crater 2, made by a single particle of $MgSiO_3$ for which the D_p/D_c ratio is close to the average value measured for pyroxene in the Kearsley et al. (2007b) calibration. For crater 1, which was formed by a pyrrhotite-bearing impactor, the D_p/D_c ratio is 20% lower. For crater 5 (mixture of olivine, sulfide and metal), the Dp/Dc ratio is equal to 0.56, again about 20% lower than the expected ratio according to the residue mineralogy. For the five others (craters 3, 4, 6, 7, 8) the D_p/D_c ratios are very close to 0.4 (from 0.38 to 0.42), which would correspond to a density of ~0.8–1 g cm^{-3} for the five impactors, according to the calibration curve of Kearsley et al. (2007b). These low values strongly suggest that most impactors were porous materials, consistent with loosely bound aggregates of <1 µm in size for most of the Wild 2 dust, as already inferred from the morphology of craters and aerogel penetration tracks by e.g., Brownlee et al. (2006), Hörz et al. (2006), and Zolensky et al. (2006). Similar conclusions were also reached by the detailed morphologic and compositional analysis of Stardust craters >50 µm (Kearsley et al. 2008).

What Proportion of the Impactor Has Been Retained Within the Craters?

The FIB sections may allow an estimate of the residue volume. For craters having a simple hemispherical geometry (such as craters 3 and 8) we constructed two spheres, one tangential to the aluminium/residue interface, and the other to the upper interface. These two spheres intercept each other and define two spherical caps, each of a well defined volume. Their subtraction gives an estimate of the residue volume. Details of comparable calculations are given in Kearsley et al. (2007a). For simplicity in our calculation to estimate the maximum retained quantity, because the FIB section sampled only a small part of the crater (typically 10%, in the central region), we assumed a centrosymmetric distribution of residue, although we can see from secondary electron images of larger craters and even from FIB sections that this is not necessarily the case in many craters. For craters having more complex morphologies, we have measured the surface area of each residue on the TEM micrographs. Their surface areas were compared to those of craters of simple morphologies and the corresponding residue volume is estimated (Table 4). No porosity has been found in these very small crater residues, so their density is probably close to that of the dominant mineral. In parallel, the projectile diameter has also been calculated from the crater diameter (using an impactor density correction deduced from the crater depth/diameter ratio of Kearsley et al. 2007b), and then the volume of the

Table 4. Summary of the dimensional measurements performed on craters. The table includes crater diameters, depths, measured residue volume, and its corresponding calculated original size and the expected original mineralogy of the projectile.

	D_c (mm)[a]	D_p (mm)[b]	D_p/D_c	ρ (g cm^{-3})[c]	P.D.1 (μm)[d]	Vol. res. (mm^3)[e]	P.D.2 (mm)[f]	Mineralogy and vol% of phases[g]
Crater #1	1.45	0.76	0.52	2.5	0.31	0.016	0.39	100% pyrrhotite
Crater #2	1.06	0.61	0.57	3.3	0.20	0.023	0.36	Single $MgSiO_3$ particle
Crater #3	1.68	0.67	0.40	0.8	0.68	0.048	0.73	Mainly olivine Fo_{93} (70%), 15% of a SiO_2-rich material, 15% Fe sulfide + metal
Crater #4	1.59	0.72	0.42	1.2	0.49	0.066	0.71	Highly dominated by pyroxene (80%), minor olivine (10%) and Fe sulfide + metal (10%)
Crater #5	1.66	0.94	0.57	3.3	0.32	0.083	0.54	Forsterite + Fe sulfides
Crater #6	2.05	0.78	0.38	0.7	0.92	0.044	0.75	Olivine + Fe sulfides
Crater #7	1.44	0.58	0.40	0.8	0.58	0.021	0.56	70% of silicates (mixture olivine + pyroxene), 30% of Fe-Zn sulfide
Crater #8	3.06	1.28	0.40	0.8	1.24	0.087	0.90	Olivine Fo_{83}

[a]Measured diameter of crater on the TEM images, from lip to lip. Some of the craters are significantly smaller than measured under the SEM (e.g., craters #2, 6, and 7). This is probably due to the fact that the corresponding TEM sections were not extracted exactly at the middle.

[b]Measured depth of the crater, from the initial surface, vertically to the top side of the residue.

[c]The density has been estimated from the calibration curve which give the ratio in function of the impactor density, from Kearsley et al. (2007b; Fig. 3a).

[d]The projectile diameter (P.D.1) is deduced from the calibration curve of Kearsley et al. (2007b; Fig. 4) which link the crater diameter/projectile versus the projectile density.

[e]The residue volume has been measured on the TEM images for craters having a semi-spherical shape (craters #3 and 8), see text for details. For others, they have been recalculated using surface measurements of the residues on the TEM images.

[f]The projectile diameter (P.D.2) deduced from the residue volume has been calculated, assuming a density of the dominant mineral, and corrected by the density deduced from the D_p/D_c ratio.

[g]Phase proportion has been estimated with surface estimation measurements on the TEM samples.

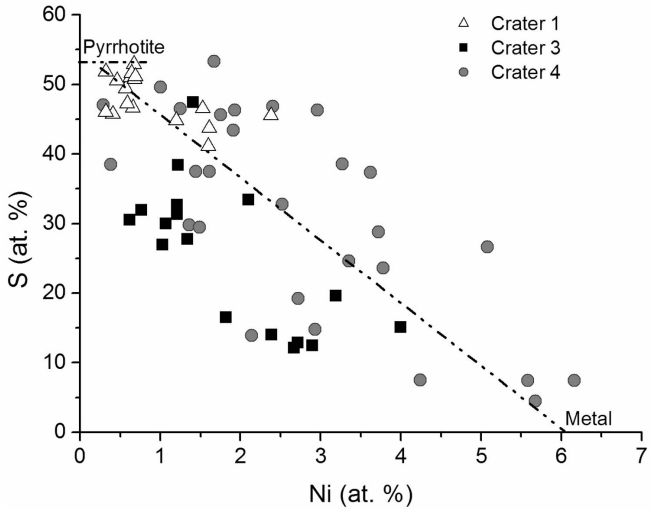

Fig. 12. S versus Ni concentrations in the Fe-Ni-S fraction of craters 1, 3, and 4. These elements are anticorrelated suggesting the presence of Fe sulfide and metal containing Ni.

projectile can be calculated based upon a simple sphere model (Table 4). These calculations should be considered as rough estimates, but the projectile sizes deduced from the ratio crater diameter and by the measurement of the residue volume are of the same order. It suggests that the majority of the impactor was retained and was not lost by volatilization or ejection of melt during the Stardust impacts at 6.1 km/s.

Loss of Volatiles During Hypervelocity Capture

Substantial S loss from Stardust penetration tracks in aerogel has been reported by Flynn et al. (2006) and has been observed in laboratory crater experiments (e.g., Kearsley et al. 2007b). Crater 1 is well suited to address this topic since it was likely formed by a pyrrhotite impactor (only S, Fe, and minor Ni were detected). Its average composition suggests that 10% of S atoms have been lost during the impact. For the other craters (3, 4, 5) the Fe:S ratio is much higher, but so is the Ni concentration. The exceptionally fine scale of the microstructures in the crater residues prevented a quantitative characterization of all Fe-Ni-S component(s). EDS measurements indicated highly variable compositions, allowing no indication on an eventual loss of S during the impact. Figure 12 summarizes these measurements for the Fe-Ni-S rich areas in craters 1, 3, and 4. For craters 3 and 4, this curve shows that S and Ni are anticorrelated suggesting that the Fe-Ni-S fraction is composed of Ni-poor sulfide and Fe,Ni metal grains. Similar trends have been found in the Fe-Ni-S inclusions in the glassy matrix of thermally modified dust particles enclosed in molten aerogel (Leroux et al. 2008). This mixing line could be indicative of the presence of metal in the impactors, associated with Fe-sulfide. On the other hand, for craters, it could be due also to strong S loss (~70 and 50% of the S atoms for crater 3 and 4, respectively), and further decomposition into metal and sulfide followed the S loss.

Is Primary Mineralogy Preserved?

The understanding of crater formation in metallic substrates has benefited greatly from studies of spacecraft surfaces returned from low Earth orbit (LEO), such as the Long Duration Exposure Facility (LDEF). The hypervelocity capture of micrometeoroids on the aluminium foil surfaces of LDEF resulted in thermal and shock alteration of the original projectiles. As a result, the impact generated craters were lined with glassy melt residues (e.g., Bernhard et al. 1993a, 1993b). However, some LDEF craters preserve pristine crystalline grains that have fragile structures such as solar flare tracks indicating they are primary minerals rather than a product of secondary recrystallization (Rietmeijer and Blanford 1988; Brownlee et al. 1993) although recrystallization was observed in other impact crater residues (Zolensky et al. 1994). Experimental light gas gun studies also provided information on the state of residue preservation including crystalline grains (Hörz et al. 1983; Kearsley et al. 2007b). However for the size-range of Stardust craters discussed in this paper, it has not yet been possible to perform laboratory simulations using projectiles that contain a well-known mixture of sub-micron silicates and nanoscale sulfides for direct comparison, due to difficulties in both producing and accelerating such a mixture.

Impacts onto the Stardust collector occurred at 6.1 km s^{-1}. Under these conditions the associated peak pressure for impacts on Al foil is of the order of 60–70 GPa for, e.g., dense olivine or pyroxene (Marsh 1980), and the temperature may reach 1000–1500 °C for monomineralic silicate projectiles (O'Keefe and Ahrens 1977; Hörz and Schaal 1981; Bernhard et al. 1993b). Temperatures can be significantly higher in the case of porous projectiles (e.g., Kieffer 1975; Ahrens and Cole 1974). The P-T ranges are sufficient to cause shock deformation and at least partial melting, but insufficient to vaporize most silicate minerals. For small particles the energy is liberated in a very short time scale (nanoseconds). Also because of the small size of the impactor, the high thermal conductivity of aluminium favors a rapid quench of the impacted products, and thus the retention of residue in the crater walls. Quenching might be especially rapid for small micron-sized craters for which the heat dissipation might be quasi-instantaneous. This is probably the reason why the amounts of residue calculated from our TEM thin sections are significant, suggesting that ejection of melted material or vapor loss did not occur. Our observations show that most of the residue melts are lining the crater floor and occasionally the lateral walls. Very frequently the elemental distribution is highly heterogeneous in residues, showing that mixing did not occur significantly between the different melted components of the incident particles, even where their melts might have been highly miscible. This heterogeneity confirms the high quench rate expected from these thin residues in contact with a metallic substrate. Crystalline grains are frequent within the melt (craters #3, 4, 5, and 8). Both craters 3 and 5 contain relatively large crystalline olivine grains composed of small domains that are slightly rotated relative to each other. This microstructure is typical of shock deformation but not of crystallization originating from melt, and thus we conclude that these grains have retained the primary mineralogy but not the microstructure of the comet. It must be remembered that the formation of sub-micron, slightly misoriented domains is typical for strongly shocked olivine (e.g., Langenhorst and Greshake 1999). Of course, we do not exclude the possibility that full melting could have occurred in other residues. For instance, the rounded grains of pyroxene visible in the residue of crater #4 (Fig. 6a) probably originate from crystallization from the melt. Residue in crater #2 clearly escaped from melting because there is no evidence for flow. The geometry is compatible with an implanted grain into aluminium.

How Do Our Results Compare with Grains in Aerogel?

Studies of small craters give access to a size population of cometary particles smaller than those currently extracted and studied from the aerogel collector. In small craters the residues probably originated from isolated submicron grains or very loosely bound dust aggregates ejected from Wild 2. Our TEM analyses of the residues show a predominance of silicates and sulfides. The incident cometary particles were monomineralic in some cases and contained a limited number of phases in others. The numerous crystalline remnants in the shock melts suggest that most of the grains were initially crystalline. The compositions of the amorphous materials (melted grains) are also mainly compatible with precursor minerals such as olivine or pyroxene. The observed mineralogy and compositions show that the small impactors consisted of a similar suite of minerals as seen in the aerogel tracks produced by larger impactors (Zolensky et al. 2006). Crystalline minerals were thus present also in the loosely bound dust aggregates or isolated Wild 2 submicron particles.

SUMMARY AND FUTURE WORK

The primary motivation for the study of micron-sized craters in the Stardust aluminium foils is the access to isolated sub-micron particles, which is impeded in the aerogel collectors, due to capture alteration and difficulty in extraction. The lack of mixing with silica aerogel is a significant advantage for determining silicate compositions. The craters are easily identified by secondary electron imaging surveys of the aluminium surface (Kearsley et al. 2008), enabling subsequent FIB extraction and TEM studies. The residues preserved within these craters provide additional and important source of comet Wild 2 material for further scientific investigations.

Our TEM studies show that micron sized Stardust craters contain substantial quantities of residue, in at least some of which the original mineralogy can be demonstrated unambiguously, as they consist of relict crystalline minerals as well as quenched melts. These residues show significant compositional diversity, indicating that they originated from

monomineralic cometary grains or composite grains that contained a limited number of phases. They differ from craters formed by larger aggregate grains, which may contain very diverse polymineralic melts (Kearsley et al. 2008). Results from the limited number of craters prepared for TEM during PE has not yet rivalled the diversity of the coarser grains trapped in aerogel tracks, from which an extraordinary mineralogical inventory can be listed (Zolensky et al. 2006). Nevertheless, the relict mineral compositions are consistent with the dominant grain types found in the aerogel tracks (Zolensky et al. 2006). The eight craters in this study did not contain detectable carbonaceous matter, but future investigation of a suite of craters that appear to contain C at levels detectable by SEM-EDS is planned.

Although FIB preparation and TEM studies are time consuming, they provide the only practical way to investigate impacting cometary particles comprised of individual submicron grains. The techniques will also greatly improve interpretation of the apparently non-stoichiometric residues in larger craters, where SEM based conventional EDS cannot resolve fine scale of compositional heterogeneity. FIB and TEM will be also vital for analysis of grains collected in the Al foils of the interstellar side of the Stardust collector.

Acknowledgments—H. L. and J. B. thank the CNES (Centre National des Etudes Spatiales) for financial support. HL thanks funding of the electron microscope facility by European FEDER and region Nord-Pas-de-Calais. RMS acknowledges support from the Office of Naval Research, and the NASA Stardust PE and SRLIDAP programs. This work was performed in part under the auspices of the U.S. Department of Energy, National Nuclear Security Administration by the University of California, Lawrence Livermore National Laboratory under contract No. W-7405-Eng-48. Z. R. D., G. A. G., and J. P. B. acknowledge support from NASA cosmochemistry, Stardust participating guest and SRLIDAP programs. The authors thank Adrian Brearley and Martin Lee for their detailed reviews and constructive comments on the manuscript. Careful editorial work by Christian Koeberl was appreciated.

Editorial Handling—Dr. Christian Koeberl

REFERENCES

Amari S., Foot J., Simon C., Swan P., Walker R. M., Jessberger E. K., Lange G., and Stadermann F. J. 1991. SIMS chemical analysis of extended impact features from the trailing edge portion of experiment AO187-2. In *LDEF Post-Retrieval Symposium*, edited by Levine A. NASA CP Technical Report 3134. pp. 503–516.

Ahrens T. J. and Cole D. M. 1974. Shock compression and adiabatic release of lunar fines from Apollo 17. Proceedings, Fifth Lunar Science Conference. pp. 2333–2345.

Barrett R. A., Zolensky M. E., Hörz F., Lindstrom D., and Gibson E. K. 1992. Suitability of SiO_2 aerogel as a capture medium for interplanetary dust. Proceedings, 22nd Lunar and Planetary Science Conference. pp. 203–212.

Bernhard R. P., Durin C., and Zolensky M. E. 1993a. Scanning electron microscopy/energy dispersive X-ray analysis of impact residues in LDEF tray clamps. In *LDEF—69 Months in Space*, edited by Levine A. NASA CP Technical Report 3194. pp. 541–549.

Bernhard R. P., See T. H., and Hörz F. 1993b. Projectiles compositions and modal frequencies on the "Chemistry of Micrometeoroids" LDEF experiment. In *LDEF—69 Months in Space*, edited by Levine A. NASA CP Techical Report 3194. pp. 551–573.

Brownlee D. E., Joswiak D., Bradley J., and Hörz F. 1993. Interplanetary meteoroid debris in LDEF metal craters. In *LDEF—69 Months In Space*, edited by Levine A. NASA CP Techical Report 3194. pp. 577–584.

Brownlee D., Tsou P., Aléon J., Alexander C. M. O'D., Araki T., Bajt S., Baratta G. A., Bastien R., Bland P., Bleuet P., Borg J., Bradley J. P., Brearley A., Brenker F., Brennan S., Bridges J. C., Browning N. D., Brucato J. R., Bullock E., Burchell M. J., Busemann H., Butterworth A., Chaussidon M., Cheuvront A., Chi M., Cintala M. J., Clark B. C., Clemett S. J., Cody G., Colangeli L., Cooper G., Cordier P., Daghlian C., Dai Z., D'Hendecourt L., Djouadi Z., Dominguez G., Duxbury T., Dworkin J. P., Ebel D. S., Economou T. E., Fakra S., Fairey S. A. J., Fallon S., Ferrini G., Ferroir T., Fleckenstein H., Floss C., Flynn G., Franchi I. A., Fries M., Gainsforth Z., Gallien J.-P., Genge M., Gilles M. K., Gillet Ph., Gilmour J., Glavin D. P., Gounelle M., Grady M. M., Graham G. A., Grant P. G., Green S. F., Grossemy F., Grossman L., Grossman J. N., Guan Y., Hagiya K., Harvey R., Heck P., Herzog G. F., Hoppe P., Hörz F., Huth J., Hutcheon I. D., Ignatyev K., Ishii H., Ito M., Jacob D., Jacobsen C., Jacobsen S., Jones S., Joswiak D., Jurewicz A., Kearsley A. T., Keller L. P., Khodja H., Kilcoyne A. L. D., Kissel J., Krot A., Langenhorst F., Lanzirotti A., Le L., Leshin L. A., Leitner J., Lemelle L., Leroux H., Liu M.-C., Luening K., Lyon I., MacPherson G., Marcus M. A., Marhas K., Marty B., Matrajt G., McKeegan K., Meibom A., Mennella V., Messenger K., Messenger S., Mikouchi T., Mostefaoui S., Nakamura T., Nakano T., Newville M., Nittler L. R., Ohnishi I., Ohsumi K., Okudaira K., Papanastassiou D. A., Palma R., Palumbo M. E., Pepin R. O., Perkins D., Perronnet M., Pianetta P., Rao W., Rietmeijer F. J. M., Robert F., Rost D., Rotundi A., Ryan R., Sandford S. A., Schwandt C. S., See T. H., Schlutter D., Sheffield-Parker J., Simionovici A., Simon S., Sitnitsky I., Snead C. J., Spencer M. K., Stadermann F. J., Steele A., Stephan T., Stroud R., Susini J., Sutton S. R., Suzuki Y., Taheri M., Taylor S., Teslich N., Tomeoka K., Tomioka N., Toppani A., Trigo-Rodríguez J. M., Troadec D., Tsuchiyama A., Tuzzolino A. J., Tyliszczak T., Uesugi K., Velbel M., Vellenga J., Vicenzi E., Vincze L., Warren J., Weber I., Weisberg M., Westphal A. J., Wirick S., Wooden D., Wopenka B., Wozniakiewicz P., Wright I., Yabuta H., Yano H., Young E. D., Zare R. N., Zega T., Ziegler K., Zimmermann L., Zinner E., and Zolensky M. 2006. Comet 81P/Wild 2 under a microscope. *Science* 314:1711–1716.

Burchell M. J., Creighton J. A., Cole M. J., Mann J., and Kearsley A. T. 2001. Capture of particles in hypervelocity impacts in aerogel. *Meteoritics & Planetary Science* 36:209–221.

Burchell M. J., Graham G. A., and Kearsley A. T. 2006. Cosmic dust collection in Aerogel. *Annual Reviews of Earth and Planetary Science* 34:385–418.

Graham G. A., McBride N., Kearsley A. T., Drolshagen G., Green S. F., McDonnell J. A. M., Grady M. M., and Wright I. P. 2001. The chemistry of micrometeoroid and space debris remnants

captured on Hubble Space telescope solar cells. *International Journal of Impact Engineering* 26:263–274.

Graham G. A., Teslich N., Dai Z., Bradley J. P., Kearsley A. T., and Hörz F. P. 2006. Focused ion beam recovery of hypervelocity impact residue in experimental craters on metallic foils. *Meteoritics & Planetary Science* 41:159–165.

Heaney P. J., Vicenzi E. P., Giannuzzi L. A., and Livi K. J. T. 2001. Focused ion beam milling: A method of site-specific sample extraction for microanalysis of Earth and planetary materials. *American Mineralogist* 86:1094–1099.

Hörz F. and Schaal R. B. 1981. Asteroidal agglutinate formation and implications for asteroidal surfaces. *Icarus* 46:337–353.

Hörz F., Fechtig H., Janicke J., and Schneider E. 1983. Morphology and projectile residue in small experimental craters. *Journal of Geophysical Research* 88:353–363.

Hörz F., Bernhard R. P., See T. H., and Brownlee D. E. 1993. Natural and orbital debris particles on LDEF's trailing and forward-facing surfaces. In *LDEF—69 Months in Space*, edited by Levine A. NASA CP Technical Report 3275. pp. 415–429.

Hörz F., Zolensky M. E., Bernhard R. P., and See T. H. 2000. Impact features and projectile residues in aerogel exposed on Mir. *Icarus* 147:559–579.

Hörz F., Bastien R., Borg J., Bradley J. P., Bridges J. C., Brownlee D. E., Burchell M. J., Chi M., Cintala M. J., Dai Z. R., Djouadi Z., Dominguez G., Economou T. E., Fairey S. A. J., Floss C., Franchi I. A., Graham G. A., Green S. F., Heck P., Hoppe P., Huth J., Ishii H., Kearsley A. T., Kissel J., Leitner J., Leroux H., Marhas K., Messenger K., Schwandt C. S., See T. H., Snead C., Stadermann F. J., Stephan T., Stroud R., Teslich N., Trigo-Rodríguez J. M., Tuzzolino A. J., Troadec D., Tsou P., Warren J., Westphal A., Wozniakiewicz P., Wright I., and Zinner E. 2006. Impact features on Stardust: Implications for comet 81P/Wild 2 dust. *Science* 314:1716–1719.

Ferreyra E., Murr L. E., Garcia E. P., and Hörz F. 1997. Effect of initial microstructure on high-velocity and hypervelocity impact cratering and crater-related microstructures in thick copper targets, Part I: Soda-lime glass projectiles. *Journal of Material Science* 32:2573–2585.

Flynn G. J., Bleuet P., Borg J., Bradley J. P., Brenker F. E., Brennan S., Bridges J., Brownlee D. E., Bullock E. S., Burghammer M., Clark B. C., Dai Z. R., Daghlian C. P., Djouadi Z., Fakra S., Ferroir T., Floss C., Franchi I. A., Gainsforth Z., Gallien J.-P., Gillet Ph., Grant P. G., Graham G. A., Green S. F., Grossemy F., Heck P. R., Herzog G. F., Hoppe P., Hörz F., Huth J., Ignatyev K., Ishii H. A., Janssens K., Joswiak D., Kearsley A. T., Khodja H., Lanzirotti A., Leitner J., Lemelle L., Leroux H., Luening K., MacPherson G. J., Marhas K. K., Marcus M. A., Matrajt G., Nakamura T., Nakamura-Messenger K., Nakano T., Newville M., Papanastassiou D. A., Pianetta P., Rao W., Riekel C., Rietmeijer F. J. M., Rost D., Schwandt C. S., See T. H., Sheffield-Parker J., Simionovici A., Sitnitsky I., Snead C. J., Stadermann F. J., Stephan T., Stroud R. M., Susini J., Suzuki Y., Sutton S. R., Taylor S., Teslich N., Troadec D., Tsou P., Tsuchiyama A., Uesugi K., Vekemans B., Vicenzi E. P., Vincze L., Westphal A. J., Wozniakiewicz P., Zinner E., and Zolensky M. E. 2006. Elemental compositions of comet 81P/Wild 2 samples collected by Stardust. *Science* 314: 1731–1735.

Kearsley A. T., Burchell M. J., Hörz F., Cole M. J., and Schwandt C. S. 2006. Laboratory simulation of impacts on aluminium foils of the Stardust spacecraft: Calibration of dust particle size from comet Wild 2. *Meteoritics & Planetary Science* 41:167–180.

Kearsley A. T., Graham G. A., McDonnell J. A. M., Taylor E. A., Drolshagen G., Chater R. J., McPhail D., and Burchell M. J. 2007a. The chemical composition of micrometeoroids impacting upon the solar arrays of the Hubble Space Telescope. *Advances in Space Research* 39:590–604.

Kearsley A. T., Graham G. A., Burchell M. J., Cole M. J., Dai, Z. R., Teslich N., Bradley J. P., Chater R., Wozniakiewicz P. A., Spratt J., and Jones G. 2007b. Analytical scanning and transmission electron microscopy of laboratory impacts on Stardust aluminum foils: Interpreting impact crater morphology and the composition of impact residues. *Meteoritics & Planetary Science* 42:191–210.

Kearsley A. T., Borg J., Graham G. A., Burchell M. J., Cole M. J., Leroux H., Bridges J. C., Hörz F., Wozniakiewicz P. J., Bland P. A., Bradley J. P., Dai Z. R., Teslich N., Westphal A., See T., Hoppe P., Heck P. R., Huth J., Stadermann F. J., Floss C., Marhas K., Stephan T., and Leitner J. 2008. Dust from comet Wild 2: Interpreting particle size, shape, structure, and composition from impact features on the Stardust aluminum foils. *Meteoritics & Planetary Science* 43. This issue.

Kieffer S. W. 1975. From regolith to rock by shock. *The Moon* 13: 301–320.

Kotula P. G., Keenan M. R., and Michael J. R. 2003. Automated analysis of SEM X-ray spectral images: A powerful new microanalysis tool. *Microscopy and Microanalysis* 9:1–17.

Kotula P. G. and Keenan M. R. 2006. Application of multivariate statistical analysis to STEM X-ray spectral images: Interfacial analysis in microelectronics. *Microscopy and Microanalysis* 12: 538–544.

Langenhorst F. and Greshake A. 1999. A transmission electron microscope study of Chassigny: Evidence for strong shock metamorphism. *Meteoritics & Planetary Science* 34:143–48.

Lee M. R., Bland P. A., and Graham G. A. 2003. Preparation of TEM samples by focused ion beam (FIB) techniques: Applications to the study of clays and phyllosilicates in meteorites. *Mineralogical Magazine* 67:581–592.

Leroux H., Borg J., Troadec D., Djouadi Z., and Hörz F. P. 2006. Microstructural study of micron-sized craters simulating Stardust impacts in aluminum 1100 targets. *Meteoritics & Planetary Science* 41:181–196.

Leroux H., Rietmeijer F. J. M., Velbel M. A., Brearley A. J., Jacob D., Langenhorst F., Bridges J. C., Zega T. J., Stroud R. M., Cordier P., Harvey R. P., Lee M., Gounelle M., and Zolensky M. E. 2008. A TEM study of thermally modified comet 81P/Wild 2 dust particles by interactions with the aerogel matrix during the Stardust capture process. *Meteoritics & Planetary Science* 43. This issue.

Marsh S. P. 1980. *LASL shock Hugoniot data*. Berkeley: University of California Press. 658 p.

Murr L. E., Quinones S. A., Ferreyrat E., Ayala A., Valerio O. L., Hörz F., and Bernhard R. P. 1998. The low-velocity-to-hypervelocity penetration transition for impact craters in metal targets. *Materials Science and Engineering A* 256:166–182.

O'Keefe J. D. and Ahrens T. J. 1977. Impact-induced energy partitioning, melting, and vaporization on terrestrial planets. Proceedings, 8th Lunar Science Conference. pp. 3357–3374.

Rietmeijer F. J. M. and Blanford G. E. 1988. Capture of an olivine micrometeoroid by spacecraft in low Earth orbit. *Journal of Geophysical Research* 93:11943–11948.

Sekanina Z. and Yeomans D. K. 1985. Orbital motion, nucleus precession, and splitting of periodic comet Brooks 2. *The Astronomical Journal* 90:2335–2352.

Stroud R. M., Nittler L. R., and Alexander C. M. O'D. 2004. Polymorphism in presolar Al_2O_3 from asymptotic giant branch stars. *Science* 305:1455–1457.

Tsou P., Brownlee D. E., Anderson J. D., Bhaskaran S., Cheuvront

A. R., Clark B. C., Duxbury T., Economou T., Green S. F., Hanner M. S., Hörz F., Kissel J., McDonnell J. A. M., Newburn R. L., Ryan R. E., Sandford S. A., Sekanina Z., Tuzzolino A. J., Vellinga J. M., and Zolensky M. E. 2004. Stardust encounters comet 81P/Wild 2. *Journal of Geophysical Research* 109, doi:10.1029/2004JE002317.

Van Cappellen E. 1990. The parameterless correction method in X-ray microanalysis. *Microscopy Microanalysis Microstructure* 1:1–22

Van Cappellen E. and Doukhan J. C. 1994. Quantitative transmission X-ray microanalysis of ionic compounds. *Ultramicroscopy* 53:343–349.

Warren J. L., Zook H. A., Allton J. H., Clanton U. S., Dardano C. B., Holder J. A., Marlow R. R., Schultz R. A., Watts L. A., and Wentworth S. J. 1989. The detection and observation of meteoroid and space debris impact features on the Solar Max Satellite. Proceedings, 19th Lunar and Planetary Science Conference. pp. 641–657.

Zega T. J., Nittler L. R., Busemann H., Hoppe P., and Stroud R. M. 2007. Coordinated isotopic and mineralogic analyses of planetary materials enabled by in situ lift-out with a focused ion beam scanning electron microscope. *Meteoritics & Planetary Science* 42:1373–1386.

Zolensky M. E., Hörz F., See T., Bernhard R. P., Dardano C., Barrett R. A., Mack K., Warren J. L., and Kinard W. H. 1994. Meteoroid investigations using the Long Duration Exposure Facility. In *Analysis of interplanetary dust*, edited by Zolensky M. E., Wilson T. L., Rietmeijer F. J. M., and Flynn G. New York: AIP Press. pp. 291–304.

Zolensky M. E., Zega T. J., Yano H., Wirick S., Westphal A. J., Weisberg M. K., Weber I., Warren J. L., Velbel M. A., Tsuchiyama A., Tsou P., Toppani A., Tomioka N., Tomeoka K., Teslich N., Taheri M., Susini J., Stroud R., Stephan T., Stadermann F. J., Snead C. J., Simon S. B., Simionovici A., See T. H., Robert F., Rietmeijer F. J. M., Rao W., Perronnet M. C., Papanastassiou D. A., Okudaira K., Ohsumi K., Ohnishi I., Nakamura-Messenger K., Nakamura T., Mostefaoui S., Mikouchi T., Meibom A., Matrajt G., Marcus M. A., Leroux H., Lemelle L., Le L., Lanzirotti A., Langenhorst F., Krot A. N., Keller L. P., Kearsley A. T., Joswiak D., Jacob D., Ishii H., Harvey R., Hagiya K., Grossman L., Grossman J. N., Graham G. A., Gounelle M., Gillet Ph., Genge M. J., Flynn G., Ferroir T., Fallon S., Ebel D. S., Dai Z. R., Cordier P., Clark B., Chi M., Butterworth A. L., Brownlee D. E., Bridges J. C., Brennan S., Brearley A., Bradley J. P., Bleuet P., Bland P. A., and Bastien R. 2006. Mineralogy and petrology of comet 81P/Wild 2 nucleus samples. *Science* 314:1735–1739.